The Astrophysical Journal Letters, 871:L15 (5pp), 2019 January 20 https://doi.org/10.3847/2041-8213/aafdb1

A Comparison between Magnetic Field Directions Inferred from *Planck* and Starlight Polarimetry toward Gould Belt Clouds

Qilao. Gu and Hua-b. Li
Department of Physics, The Chinese University of Hong Kong, Shatin, New Territory, Hong Kong, People's Republic of China; qlgu@phy.cuhk.edu.hk, hbli@cuhk.edu.hk
Received 2018 July 5; revised 2019 January 7; accepted 2019 January 10; published 2019 January 23

Abstract

We compare the magnetic field (*B*-field) orientations inferred from *Planck* 353 GHz thermal dust polarization and starlight polarimetry data and study the cloud-field alignment based on these two tracers within Gould Belt clouds, which show good agreement with each other. Furthermore, we analyze two fundamentally different alignment studies—global (cloud scale, ∼10–100 pc) cloud-field alignment, which compares mean fields and global cloud orientations, and local (pixel size scale, ∼0.1–1 pc) structure-field alignment, which compares this relation pixel by pixel—and find the connection between them.

Key words: infrared: ISM – ISM: clouds – magnetic fields – polarization – submillimeter: ISM

1. Introduction

The polarization of starlight extinction and thermal emission due to interstellar dust have been extensively used to study the orientations of the interstellar *B*-field projected on the plane of the sky (Heiles 2000; Li et al. 2014, 2015, 2017; Pillai et al. 2015; Planck Collaboration Int. XIX 2015; Pattle et al. 2017), which provides a unique point of view from which to study the role of *B*-fields in the star formation process (Crutcher 2012; Li et al. 2014). While the starlight polarization can trace the fields in the low-density inter-cloud media (ICM) and the outskirts of molecular clouds, thermal dust emission can trace the fields within a cloud. We have shown that the cloud and ICM field orientations traced by the two methods are highly correlated, which suggests that the *B*-fields are "rigid" during cloud formation (Li et al. 2009).

The rigid field orientations will inevitably leave their mark on the orientations of cloud structures, which have also recently been surveyed with both field orientation tracers (Li et al. 2013; Planck Collaboration Int. XXXV 2016). With starlight polarization (Heiles 2000), Li et al. (2013) studied the relative alignment between the global cloud orientations (derived from auto-correlation of extinction maps) and their nearby ICM fields of 13 Gould Belt clouds. They found a bimodal distribution that clouds tend to be either parallel with or perpendicular to the mean *B*-field directions of local ICM. Later, Planck Collaboration Int. XXXV (2016) found that the relative orientation between *B*-field and subcloud structures tends to move away from parallelism with increasing column density.

The comparison between the two surveys, however, can be tricky. Besides the field tracers, the two teams also used different methods to track density structures. After comparing the field orientations based on the two tracers, the connection between the two studies of the cloud-field relation is another main focus of this work. We will first repeat the study of Li et al. (2013) using *Planck*[1] thermal dust polarization data as the *B*-field tracer to see whether the two studies agree with each other. Furthermore, we try to find the connection between the two surveys by comparing the Li et al. (2013) results with the Planck Collaboration Int. XXXV (2016) results at $N_{\rm H}$, which defines the cloud shapes in the study of Li et al. (2013).

This paper is organized as follows. Section 2 introduces the *Planck* 353 GHz polarization maps and starlight polarization observations. Section 3 shows our results and provides a discussion. Finally, a summary is given in Section 4.

2. Data

2.1. 353 GHz Thermal Dust Polarization

Planck detected linearly polarized emission in seven frequency bands from 30 to 353 GHz (Planck Collaboration I 2014). We use the data from the High Frequency Instrument (HFI) at the 353 GHz band of the R2.02 release, at which the contribution of cosmic microwave background (CMB) polarized emission is negligible because it is closer to the peak wavelength of dust thermal emission (Planck Collaboration Int. XIX 2015; Planck Collaboration Int. XX 2015). The whole-sky 353 GHz maps of Stokes parameters (*I*, *Q*, *U*) together with their covariances (*II*, *IQ*, *IU*, *QQ*, *QU*, *UU*) are initially at 4.′8 resolution in HEALPix format (Górski et al. 2005). To increase the signal-to-noise ratio (S/N), we smoothed all the maps to 10′ resolution using a Gaussian approximation of the *Planck* beam and the covariance smoothing procedures described in Planck Collaboration Int. XIX (2015). We used Cartesian projection to show all the individual regions.

Based on the fact that the long axes of dust grains in interstellar media tend to be perpendicular to the orientation of the *B*-field (Lazarian 2003), the starlight polarization angle ($\theta_{\rm starlight}$) infers *B*-field orientation ($B_{\rm starlight}$) and the submillimeter polarization angle ($\theta_{\rm submm}$) is perpendicular to the inferred *B*-field orientation ($B_{\rm submm}$), thus we have $B_{\rm starlight} = \theta_{\rm starlight}$ and $B_{\rm submm} = \theta_{\rm submm} + \pi/2$. We derive $\theta_{\rm submm}$ from *Planck* data by

$$\theta_{\rm submm} = 0.5 \times \arctan(-U, Q) \quad (1)$$

to follow IAU convention, which is measured counterclockwise from the north Galactic pole in positive degrees. The

[1] *Planck* (http://www.esa.int/Planck) is a project of the European Space Agency (ESA) with instruments provided by two scientific consortia funded by ESA member states (in particular the lead countries France and Italy), with contributions from NASA (USA) and telescope reflectors provided by a collaboration between ESA and a scientific consortium led and funded by Denmark.

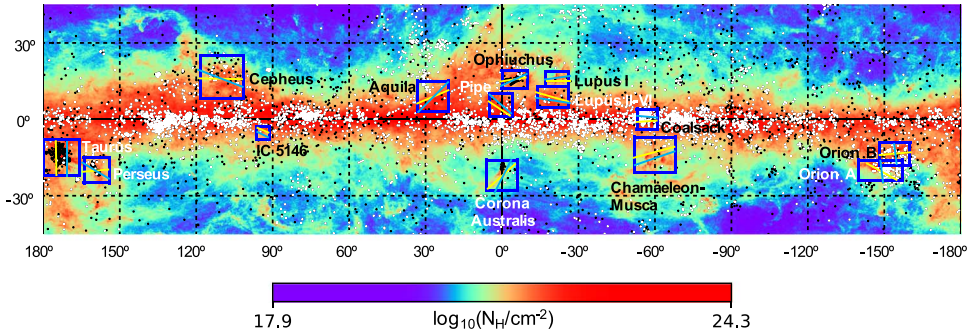

Figure 1. Spatial distribution of stars in Heiles' (2000) catalog. Black dots mark all the stars while white ones mark those with signal-to-noise ratio (S/N) $p/\sigma_p \geqslant 3$. The colors represent the total gas column density in logarithmic scale. Blue rectangles show the locations of all the Gould Belt clouds we study in this work. Blue and yellow bars show the average *B*-field orientations inferred from starlight and *Planck* 353 GHz thermal dust polarization separately ($B_{\rm starlight}$ and $B_{\rm High}$ in Table 1).

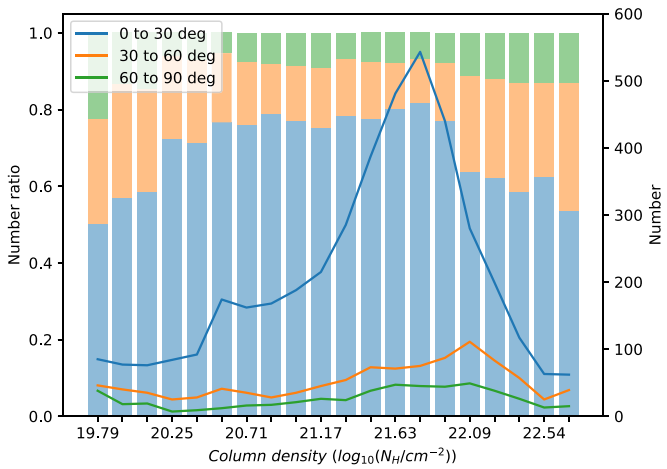

Figure 2. *Planck*-starlight inferred *B*-field orientation offsets the distribution with increasing $N_{\rm H}$. We choose stars with polarization S/N larger than 3 and ensure that every column has more than 100 stars. Blue, orange, and green columns represent small (0°–30°) difference, medium (30°–60°) difference, and big (60°–90°) difference respectively. The histogram shows the number ratios of three groups (left *y*-axis) while the line chart shows their numbers (right *y*-axis).

arctan$(-U,Q)$ function is used to compute arctan$(-U/Q)$ avoiding the π ambiguity.

2.2. Starlight Polarization

For starlight polarization, we used the catalog's agglomeration made by Heiles (Heiles 2000). It contains 9286 stars (Figure 1), 5747 of which have polarization signal-to-noise ratio (S/N) $p/\sigma_p \geqslant 3$. To compare with *Planck* data, we apply 10′ Gaussian smoothing (Section 2.1) centered at each stellar position on the *Planck* Q and U maps with 4.′8 resolution.

3. Results and Discussion

3.1. Stellar versus Planck Inferred B-field Directions

Figure 2 shows *Planck*-starlight inferred *B*-field orientation offsets versus $N_{\rm H}$, following Planck Collaboration XI (2014),

$$\frac{\tau_{353}}{N_H} = 1.2 \times 10^{-26}\,{\rm cm}^2, \quad (2)$$

where τ_{353} is *Planck* dust optical depth at 353 GHz. In general, the offsets are small, mostly below 30°. The offsets first decrease and then increase with increasing $N_{\rm H}$, showing lower alignment in low $N_{\rm H}$ and extremely high $N_{\rm H}$ regions. This result could be explained by the fact that the starlight method only traces the foreground of the targeted star while submillimeter polarization averages the entire LOS. Their overlap (the stellar foreground) is more weighted in the submillimeter-detection when the foreground $N_{\rm H}$ is higher, which explains the decreasing offsets with increasing $N_{\rm H}$. Similarly, Planck Collaboration Int. XXI (2015) found that $B_{\rm starlight}$ and B_{Planck} have a good agreement when the ratio of *Planck* inferred $E(B-V)_s$ to $E(B-V)$ is close to 1, as this ratio becomes closer to 1 while the overlap of two methods increases.

However, if the $N_{\rm H}$ is so high that the background stars start to become invisible, the visible stars are mostly in the foreground so the overlap of the submillimeter and starlight traced volumes decreases, and thus the offsets grow accordingly. Moreover, the stellar feedback may also contribute to growing the offset toward high $N_{\rm H}$ by deviating the fields in extremely high densities.

3.2. Stellar versus Planck in the Cloud-field Alignment toward Gould Belt Clouds

We repeat the cloud-field alignment study carried out by Li et al. (2013), who used starlight polarization to trace *B*-fields, but here we use the *Planck* 353 GHz data (Planck Collaboration Int. XXXV 2016). The work of Li et al. (2013) is updated in Li et al. (2017), so here we adopt the cloud regions and orientations from the latter. Planck Collaboration Int. XXXV (2016) divided each cloud region into high-, medium-, and low-$N_{\rm H}$ subregions (columns 6, 7, and 8 in Table 1) and, accordingly, we derive the mean field directions from high-, medium-, and low-$N_{\rm H}$, respectively, for each cloud. The result, the cloud-field offsets, are compared with those from Li et al. (2017), cloud by cloud, in Figure 3. The Pearson's correlation coefficients and p-values between the cloud-field offsets based on *Planck* and starlight data are (0.84, 0.0002), (0.80, 0.0005), and (0.46, 0.0988) for high-, medium-, and low-$N_{\rm H}$ respectively. The two analyses agree best in the high $N_{\rm H}$ region (Figure 3(A)), this is not a surprise if we consider how Planck Collaboration Int. XXXV (2016) defined high-density: $N_{\rm H} = 10^{21.2}$–$10^{22}{\rm cm}^{-2}$ (Table 1), which is also the density range where *Planck* and stellar inferred *B*-fields agree the best in Figure 2. Within this density, indeed we see the Li et al. (2013) type of bimodality with *Planck* data.

Table 1
Locations and Properties of the Selected Gould Belt Clouds (All Directions Are in Galactic Coordinates and Increase Counterclockwise from the North Galactic Pole)

Cloud	l (°)	b (°)	Long Axes[a] (°)	$B_{\rm starlight}$[a] (°)	$B_{\rm High}$[b] (°)	$B_{\rm Medium}$[b] (°)	$B_{\rm Low}$[b] (°)	high $N_{\rm H}$[c] $\log_{10}(N_{\rm H}/{\rm cm}^{-2})$	low $N_{\rm H}$[c] $\log_{10}(N_{\rm H}/{\rm cm}^{-2})$
IC 5146	91.3, 96.3	−8, −3	−38	64 ± 16	67^{+9}_{-7}	70^{+5}_{-6}	77^{+9}_{-8}	21.46	21.26
Pipe	−4, 5	1, 10	−45	49 ± 13	56^{+18}_{-10}	83^{+24}_{-14}	-79^{+10}_{-14}	21.78	21.46
Orion A	−157, −140	−24, −16	83	7 ± 20[d]	61^{+25}_{-22}	59^{+34}_{-39}	14^{+42}_{-19}	21.61	21.23
Orion B	−160, −148	−18, −9	−30	7 ± 18[d]	-85^{+16}_{-15}	-82^{+12}_{-9}	-87^{+11}_{-24}	21.61	21.23
Chamaeleon-Musca	−68, −52	−21, −7	19	−71 ± 11	-75^{+6}_{-6}	-75^{+7}_{-7}	-70^{+12}_{-9}	21.26	20.95
Taurus	166, 180	−22, −8	75	0 ± 18	1^{+16}_{-27}	24^{+17}_{-17}	70^{+10}_{-33}	21.64	21.25
Lupus I	−26, −17	12.7, 18.7	−1	−82 ± 13	90^{+28}_{-26}	-83^{+30}_{-29}	-88^{+12}_{-11}	21.54	21.19
Lupus II-VI	−26, −14	4.7, 12.7	−73	81 ± 11	74^{+11}_{-12}	84^{+11}_{-7}	-89^{+9}_{-9}	21.54	21.19
Corona Australis	−6, 6	−28, −16	−26	−27 ± 32	-48^{+32}_{-34}	-88^{+10}_{-12}	82^{+11}_{-11}	21.17	20.67
Coalsack	−61, −53	−4, 4	74	85 ± 6	-86^{+9}_{-11}	88^{+10}_{-8}	90^{+6}_{-7}	22.00	21.60
Cepheus	101.5, 118.5	8, 25	65	69 ± 36	89^{+16}_{-15}	72^{+12}_{-52}	53^{+17}_{-14}	21.53	21.04
Aquila	21, 33	3, 15	−75	−45 ± 10	-67^{+14}_{-9}	-54^{+8}_{-8}	-48^{+9}_{-7}	21.84	21.24
Ophiuchus	−10, 0	12, 19	−45	−65 ± 25	-81^{+9}_{-21}	-79^{+8}_{-15}	-84^{+11}_{-10}	21.53	21.23
Perseus	154, 164	−25, −15	32	59 ± 35	-85^{+13}_{-30}	72^{+31}_{-23}	84^{+9}_{-23}	21.58	21.09

Notes.
[a] Cloud long axes and $B_{\rm starlight}$ are adopted from Li et al. (2013).
[b] The mean B-field orientations are from *Planck*, $B_{\rm High}$ is derived from pixels with higher column density than high $N_{\rm H}$, $B_{\rm Low}$ is derived from pixels with lower column density than low $N_{\rm H}$, $B_{\rm Medium}$ is derived from pixels with medium column density. Superscript and subscript show the interquartile range (IQR) with setting average as Q_2 (the second quartile).
[c] High $N_{\rm H}$ and low $N_{\rm H}$ are adopted from Planck Collaboration Int. XXXV (2016).
[d] Li et al. (2013) combined Orion A and B as Orion, we separate them and calculate their $B_{\rm starlight}$ using same method as Li et al. (2013).

3.3. Outliers in Figure 3

As shown in Figure 3(A), we find Perseus and Orion A/B as outliers owing to the larger *Planck*-starlight difference, thus we take a closer look at them.

For Perseus, Goodman et al. (1990) found that the B-field orientations inferred from starlight are bimodal: vectors with low polarization fractions are mostly parallel with the cloud and those with high fractions are roughly perpendicular to the cloud (Figure 3(E)). The former group has more starlight data so the mean orientation inferred from starlight shows parallel alignment (Li et al. 2013). On the other hand, the thermal-emission method favors regions with higher polarized flux and thus weights the perpendicular directions more. Goodman et al. (1990) showed evidence that the B-fields inferred from higher-polarization vectors are shaped by the stellar feedback, so the field prior to stellar feedback should be parallel to the cloud. Also shown in Figure 3(E), the field orientation from even higher density (thus closer to the embedded stars) traced by CSO indeed aligns closer to the field traced by *Planck*, which supports the idea that the *Planck*—starlight discrepancy in Perseus is due to stellar feedback.

On the other hand, it is well known that most core fields within the Orion molecular cloud are not only aligned with each other, but also aligned with the mean field inferred from the stellar polarization within 100 pc (Li et al. 2009; Figure 3(D)). Which means that the disagreement between the Orion A/B fields traced by *Planck* and starlight cannot be simply explained by stellar feedback. Resolving this discrepancy shall improve our understanding of *Planck* polarimetry. One possible reason might be that Orion, the most massive cloud in the Gould Belt, has a more extended high $N_{\rm H}$ region along the LOS such that *Planck* traced an LOS dimension much larger than a core. Which will not happen to $B_{\rm CSO}$, whose beam is smaller than a core, and $B_{\rm starlight}$, whose LOS scale can be controlled by stellar distance.

OMC-1, the only core in the OMC that has B-fields better aligned with *Planck* data (Figure 3), has B-field orientations that are significantly deviated and aligned with the BN/KL outflow, the most energetic outflow known in a star-forming region (Pattle et al. 2017).

3.4. The Connection between Planck Collaboration Int. XXXV (2016) and Li et al. (2013)

Different from the global cloud-field alignment discussed in Section 3.2, Planck Collaboration Int. XXXV (2016) studied a different kind of cloud structure-field alignment, they studied alignment pixel by pixel: local field orientations versus local structure orientations, which are defined by 90° from the local column density gradient. The result is shown in Figure 4, an overall trend of moving away from parallelism toward perpendicularity with increasing $N_{\rm H}$. This should not be interpreted as that *Planck* high-$N_{\rm H}$ structures being all perpendicular to B-field, Figure 3(A) shows that they are not.

The probability density function (PDF) of $N_{\rm H}$ can help us better link Figure 4 with Li et al. (2013). The PDF turns from log-normal to roughly a power law where the gas turns gravitational bounded, which can be used to define the cloud threshold $N_{\rm H}$ (Kainulainen et al. 2009; Froebrich & Rowles 2010; Ward et al. 2014). The mass related to star formation is dominantly located in the power-law part of the PDF, Gould Belt clouds' $N_{\rm H}$ PDFs turn from log-normal to power-law-like at $2 < A_v < 5$ (Kainulainen et al. 2009), corresponding to $21.57 < \log_{10}(N_{\rm H}/{\rm cm}^{-2}) < 21.97$ (Bohlin et al. 1978; Vrba & Rydgren 1984), which is shown in Figure 4 as gray region. Clearly, in this density range, which defines the global cloud orientation studied in Li et al. (2013), the structure-field alignment shows both perpendicularity (blue) and parallelism (red). Figure 5 is the global cloud-field alignment adopted from Li et al. (2013); here we color the clouds with the same colors used in Figure 4 to illustrate the

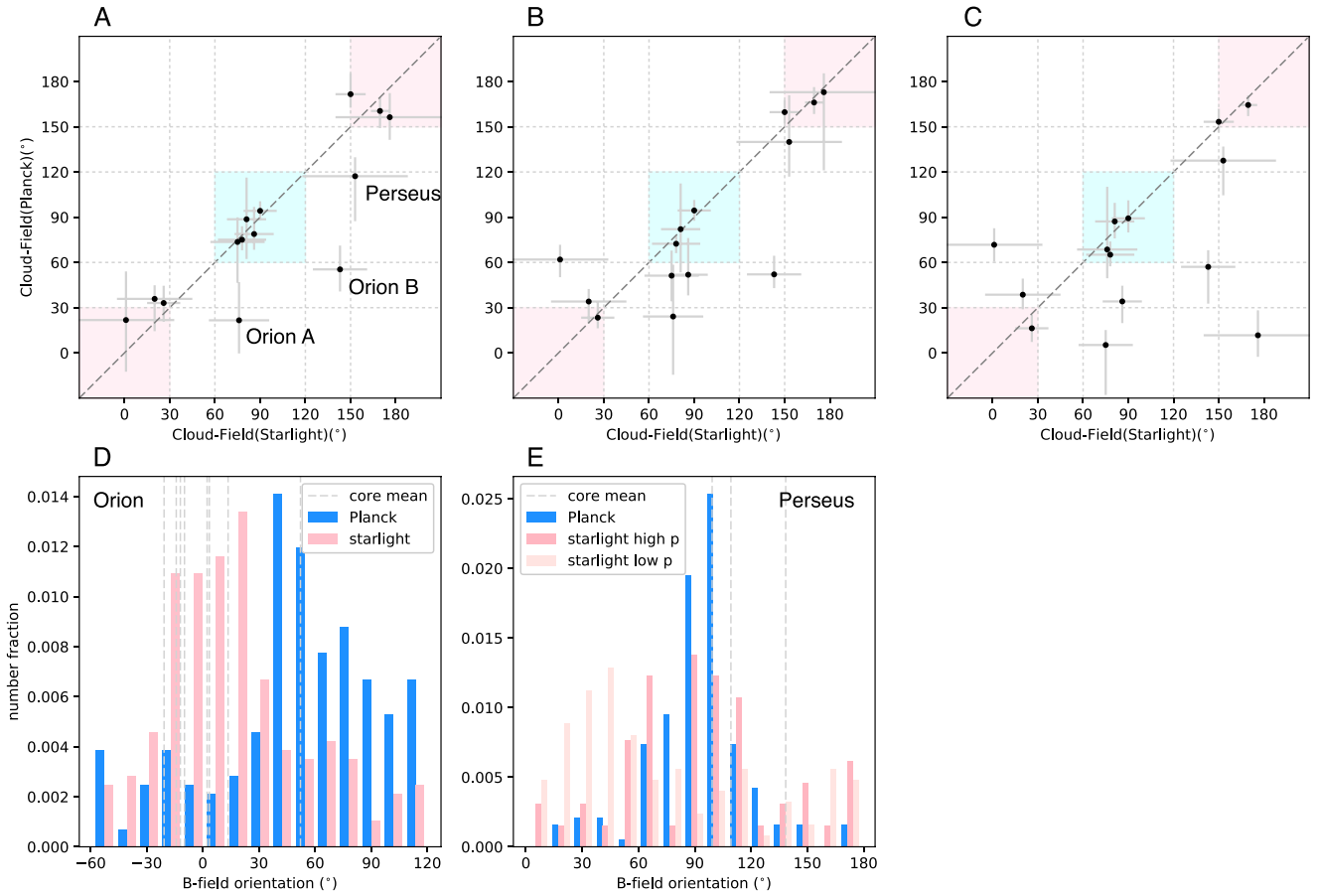

Figure 3. Upper panels: comparison of two cloud-field offsets. *B*-field orientations are inferred from *Planck* and starlight data, and cloud orientation is adopted from Li et al. (2017). Panels (A)–(C) represent the results from high-, medium-, and low-$N_{\rm H}$ regions, respectively (Table 1, following Planck Collaboration Int. XXXV 2016), and error bars show the uncertainties of *B*-field (Table 1). Dashed lines mark the regions that are within 30° from perfect parallelism/perpendicularity for reference and the red/blue shaded regions are the intersections where two offsets agree with each other. Orion and Perseus are the apparent outliers in panel (A), for which, cloud-field distributions are shown in panels (D) and (E). The starlight data (pink) from these two regions is adopted from Li et al. (2013), and the corresponding *Planck* data (blue) is derived as in Section 2.2. The core (gray; with $n_{\rm H} > 10^5$ and scale 0.1 ∼ 1pc) mean fields are adopted from Dotson et al. (2010) and Chapman et al. (2013). The only Orion core aligned better with *Planck* is OMC-1. The lighter and pink data in panel (E) stand for polarization fractions above and below 1.5%, respectively.

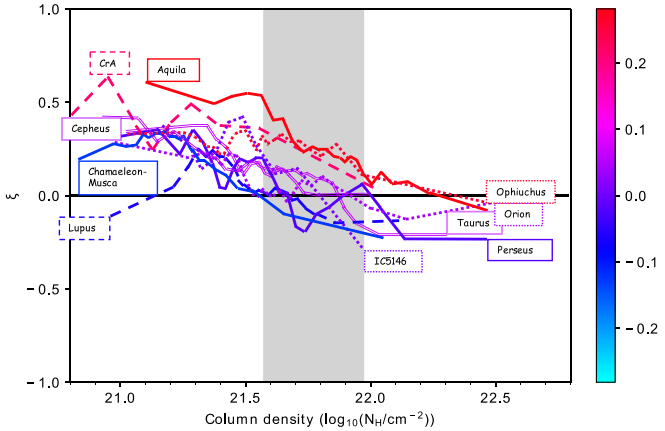

Figure 4. All clouds' ξ parameters without error bars (Planck Collaboration Int. XXXV 2016). $\xi > 0$ for *B*-field mostly aligned with $N_{\rm H}$ contours (1 for perfect parallelism), $\xi < 0$ for *B*-field mostly perpendicular to $N_{\rm H}$ contours (−1 for perfect perpendicularity), $\xi \approx 0$ for no preferred relative orientation. The gray region marks the column density that corresponds to $2 < A_v < 5$; we colored these lines according to their areas above $\xi = 0$. Red shows parallelism while blue shows perpendicularity.

connection between Figures 4 and 5. As shown in Figure 5, dots in panel $y = x$ tend to be redder while those in $y = x$–90 tend to be bluer, which shows some agreements.

4. Summary

In this work, we compare *B*-field directions inferred from *Planck* and starlight polarimetry and analyze the two cloud-field alignment relations (Planck Collaboration Int. XXXV 2016; Li et al. 2013), and we find their connection by using those *B*-field data. We reach the following conclusions:

(1) In general, *B*-field directions inferred from two methods agree well (Figure 2). The slight disagreement in low and extremely high $N_{\rm H}$ regions can be explained by the following: (a) the overlap of the LOS traced by the two methods is more weighted with higher foreground $N_{\rm H}$, (b) visible stars in extreme high $N_{\rm H}$ LOS are mostly in the foreground, which decreases the overlap of two methods, and (c) stellar feedback affects the denser regions more.

(2) Based on *Planck* 353 GHz thermal dust polarization data, we repeat the global cloud-field alignment study carried out by Li et al. (2013) and find a good agreement with high-$N_{\rm H}$ data.

(3) In the range of cloud contraction threshold density, $2 < A_v < 5$ (Kainulainen et al. 2009) where column density PDFs turn from log-normal to roughly a power law, the local cloud-field alignment observed by Planck Collaboration Int.

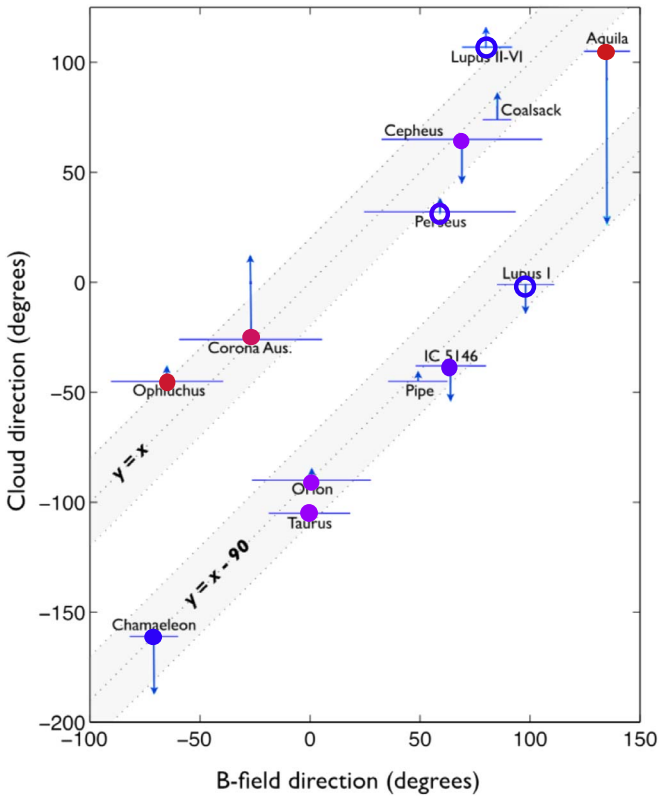

Figure 5. Cloud-field bimodal distribution from Li et al. (2013), color-coded according to Figure 4. Clouds with hollow symbols are not suitable for the comparison here. For Perseus, see the discussion in Section 3.2. In Li et al. (2013), Lupus is divided into Lupus I and Lupus II-VI, so we use hollow symbols for Lupus I and Lupus II-VI for clarity.

XXXV (2016) shows some agreements with the study of the global cloud-field alignment (Li et al. 2013; Figures 4 and 5).

For future plans, we will further this study in two aspects:

(1) Section 3.3 suggests a deeper understanding of *Planck* data is needed to explain why the core fields observed by CSO (Li et al. 2009) agree better with the field inferred from starlight data than *Planck* data.

(2) The threshold density defined by $N_{\rm H}$ PDF divides a cloud into subregions. An in-depth study of structure-field alignment on those subregions would help us better understand the role played by *B*-field in cloud fragmentation.

This work is supported by General Research Fund 14600915 from the Research Grants Council of Hong Kong.

ORCID iDs

Qilao. Gu https://orcid.org/0000-0002-2826-1902
Hua-b. Li https://orcid.org/0000-0003-2641-9240

References

Bohlin, R. C., Savage, B. D., & Drake, J. F. 1978, ApJ, 224, 132
Chapman, N. L., Davidson, J. A., Goldsmith, P. F., et al. 2013, ApJ, 770, 151
Crutcher, R. M. 2012, ARA&A, 50, 29
Dotson, J. L., Vaillancourt, J. E., Kirby, L., et al. 2010, ApJS, 186, 406
Froebrich, D., & Rowles, J. 2010, MNRAS, 406, 1350
Goodman, A. A., Bastien, P., Menard, F., & Myers, P. C. 1990, ApJ, 359, 363
Górski, K. M., Hivon, E., Banday, A. J., et al. 2005, ApJ, 622, 759
Heiles, C. 2000, AJ, 119, 923
Kainulainen, J., Beuther, H., Henning, T., & Plume, R. 2009, A&A, 508, L35
Lazarian, A. 2003, JQSRT, 79, 881
Li, H.-b., Dowell, C. D., Goodman, A., Hildebrand, R., & Novak, G. 2009, ApJ, 704, 891
Li, H.-b., Fang, M., Henning, T., & Kainulainen, J. 2013, MNRAS, 436, 3707
Li, H.-B., Goodman, A., Sridharan, T. K., et al. 2014, in Protostars and Planets VI, ed. H. Beuther et al. (Tucson, AZ: Univ. Arizona Press), 101
Li, H.-B., Jiang, H., Fan, X., Gu, Q., & Zhang, Y. 2017, NatAs, 1, 0158
Li, H.-B., Yuen, K. H., Otto, F., et al. 2015, Natur, 520, 518
Pattle, K., Ward-Thompson, D., Berry, D., et al. 2017, ApJ, 846, 122
Pillai, T., Kauffmann, J., Tan, J. C., et al. 2015, ApJ, 799, 74
Planck Collaboration I 2014, A&A, 571, A1
Planck Collaboration Int. XIX 2015, A&A, 576, A104
Planck Collaboration Int. XX 2015, A&A, 576, A105
Planck Collaboration Int. XXI 2015, A&A, 576, A106
Planck Collaboration Int. XXXV 2016, A&A, 586, A138
Planck Collaboration XI 2014, A&A, 571, A11
Vrba, F. J., & Rydgren, A. E. 1984, ApJ, 283, 123
Ward, R. L., Wadsley, J., & Sills, A. 2014, MNRAS, 445, 1575